



Saha, G., and Paul, M. C. (2017) Transition of nanofluids flow in an inclined heated pipe. *International Communications in Heat and Mass Transfer*, 82, pp. 49-62. (doi:[10.1016/j.icheatmasstransfer.2017.02.017](https://doi.org/10.1016/j.icheatmasstransfer.2017.02.017))

This is the author's final accepted version.

There may be differences between this version and the published version. You are advised to consult the publisher's version if you wish to cite from it.

<http://eprints.gla.ac.uk/135909/>

Deposited on: 31 January 2017

# Transition of Nanofluids Flow in an Inclined Heated Pipe

Goutam Saha<sup>1,a</sup> and Manosh C. Paul<sup>a,\*</sup>

<sup>a</sup>Systems, Power and Energy Research Division, School of Engineering, University of Glasgow, Glasgow G12 8QQ, UK

<sup>1</sup>Department of Mathematics, University of Dhaka, Dhaka-1000, Bangladesh.

\*Corresponding author. Tel.: +44(0)141 330 8466

Email:Manosh.Paul@glasgow.ac.uk

## Abstract

A numerical investigation is carried out to investigate the transitional flow behaviour of nanofluids flow in an inclined pipe using both single and multi-phase models. Two different nanofluids are considered, and these are  $\text{Al}_2\text{O}_3$ -water and  $\text{TiO}_2$ -water nanofluids. Moreover, SST  $\kappa - \omega$  transitional model is implemented to study the nanofluids flow in inclined pipe. Gravitational force is also adopted by considering Boussinesq approximation in the momentum equation. Results reveal that Buoyancy force play a significant role on the degeneration of heat transfer rate with the increase of Reynolds number for different inclination angles. It indicates that mixed convection has opposite effect on the inclined pipe than the forced convection on the horizontal pipe. Moreover, some deformation of the flow and temperature fields near the upstream region is observed with the increase of inclination angle due to Buoyancy force.

*Key words:* Nanofluids; heat transfer; single phase model; multi-phase model; inclined pipe.

## 1. Introduction

A numerical study has been carried out to understand the heat transfer behaviour of  $\text{Al}_2\text{O}_3$ - $\text{H}_2\text{O}$  and  $\text{TiO}_2$ - $\text{H}_2\text{O}$  nanofluids flow in an inclined pipe using both the single and multi-phase models under transition flow condition in this paper. The SST  $\kappa - \omega$  transitional model with different inclination angles from  $0^\circ$  to  $75^\circ$  has been used for simulating the transition flow regime. Previously, it was found that combination of the smaller size of nanoparticles (e.g.  $d_p = 10 \text{ nm}$ ) and the higher nanoparticles concentration ( $\chi = 6\%$ ) had produced the highest thermal performance when the Brownian motion of nanoparticles had been taken into account. Details of these findings have been discussed in Saha and Paul [1-3] respectively.

Literature review suggests that a very few experimental and numerical investigations have been carried out to date on the laminar and turbulent nanofluid flow in an inclined or a vertical pipe [4-6]. And, we are the first to have investigated the nanofluids flow inside an inclined pipe in transition regime considering a smaller size but higher concentrations (mentioned above) of nanoparticles with the Brownian motion.

## 2. Mathematical Modelling

In this research, numerical investigations have been carried out using single and multi-phase models under transition flow condition. Here, three-dimensional model of an inclined pipe with a length  $L$  of  $1.0 \text{ m}$  and a circular section with diameter  $D_h$  of  $0.019 \text{ m}$  is shown in Fig. 1.

### Single Phase Model:

The dimensional steady-state governing equations of fluid flow and heat transfer for the single phase model is presented under the following assumptions:

- i. Fluid flow is incompressible, Newtonian and transitional,
- ii. Fluid phase and nanoparticle phase are in thermal equilibrium with no-slip between them,
- iii. Nanoparticles are spherical and uniform in size and shape,
- iv. Radiation effects and viscous dissipation are negligible.

$$\nabla \cdot (\rho \vec{v}) = 0 \quad (1)$$

$$\nabla \cdot (\rho \vec{v} \vec{v}) = -\nabla p + \nabla \cdot \left[ \mu (\nabla \vec{v} + \nabla \vec{v}^T) - \frac{2}{3} \nabla \cdot \vec{v} I \right] + \rho \vec{g} \quad (2)$$

$$\nabla \cdot (\rho \vec{v} C_p T_{nf}) = \nabla \cdot (\lambda \nabla T_{nf}) \quad (3)$$

where  $\vec{v}, \rho, \mu, \lambda, \vec{g}$  are the mass-average velocity, density, viscosity, thermal conductivity and gravitational force respectively.

### Multi-Phase Mixture Model:

The dimensional steady-state governing equations of continuity, momentum, energy and concentration for the multi-phase model are presented considering the assumptions (i) to (iv) given in the single phase model. Moreover, it is assumed that there is a strong coupling between the fluid and nanoparticles phases and these phases move at the same local velocity. Interaction between the fluid and nanoparticles is also taken into account. It is also assumed that fluid and nanoparticles phases are in local thermal equilibrium in multi-phase mixture model. It means, mean temperature of the fluid phase and the nanoparticles phase are same. Moreover, the multi-phase mixture model allows the phases to move at different or same velocities using the concept of drift velocity. When the phases can also be assumed to move at same velocities then the mixture model is called the homogeneous multi-phase model. Moreover, the momentum equation for the mixture can be obtained by summing the individual momentum equations for all the phases.

Under the above assumptions, the governing equations for the multi-phase mixture model can be expressed as (Fluent [7]):

$$\nabla \cdot (\rho \vec{v}) = 0 \quad (4)$$

$$\nabla \cdot (\rho \vec{v} \vec{v}) = -\nabla p + \nabla \cdot [\mu (\nabla \vec{v} + \nabla \vec{v}^T)] + \rho \vec{g} + \nabla \cdot \left( \sum_{s=1}^n \chi_s \rho_s \vec{v}_{dr,s} \vec{v}_{dr,s} \right) \quad (5)$$

$$\nabla \cdot \left[ \sum_{s=1}^n \chi_s \vec{v}_s (\rho_s H_s + p) \right] = \nabla \cdot \left( \sum_{s=1}^n \chi_s (\lambda + \lambda_t) \nabla T_{nf} \right) \quad (6)$$

$$\nabla \cdot (\chi_p \rho_p \vec{v}) = -\nabla \cdot (\chi_p \rho_p \vec{v}_{dr,p}) \quad (7)$$

Also,  $\vec{v}, \rho, \mu, \lambda, n, \lambda_t, \chi_s$  are the mass-average velocity, mixture density, viscosity of the mixture, mixture thermal conductivity coefficient, number of phases, turbulent thermal conductivity and nanoparticles concentration respectively. These are also defined as

$$\begin{aligned}\vec{v} &= \sum_{s=1}^n \frac{\chi_s \rho_s \vec{v}_s}{\rho} & \rho &= \sum_{s=1}^n \chi_s \rho_s \\ \mu &= \sum_{s=1}^n \chi_s \mu_s & \lambda &= \sum_{s=1}^n \chi_s \lambda_s\end{aligned}$$

Here,  $H_s$  is the sensible enthalpy for phase  $s$ . The drift velocity ( $\vec{v}_{dr,s}$ ) for the secondary phase  $s$  is defined as

$$\vec{v}_{dr,s} = \vec{v}_s - \vec{v} \quad (8)$$

The relative or slip velocity is defined as the velocity of the secondary phase ( $s$ ) relative to the velocity of the primary phase ( $f$ ):

$$\vec{v}_{sf} = \vec{v}_s - \vec{v}_f \quad (9)$$

Then the drift velocity related to the relative velocity becomes

$$\vec{v}_{dr,s} = \vec{v}_{sf} - \sum_{k=1}^n \vec{v}_{fk} \frac{\chi_k \rho_k}{\rho} \quad (10)$$

Manninen *et al.* [8] and Naumann and Schiller [9] proposed the following respective equations for the calculation of the relative velocity,  $\vec{v}_{pf}$ , and the drag function,  $f_{drag}$ .

$$\vec{v}_{pf} = \frac{\rho_p d_p^2}{18\mu_f f_{drag}} \frac{\rho_p - \rho}{\rho_p} \vec{a} \quad (11)$$

$$f_{drag} = \begin{cases} 1 + 0.15 Re_p^{0.687} & Re_p \leq 1000 \\ 0.0183 Re_p & Re_p > 1000 \end{cases} \quad (12)$$

Here, the acceleration  $\vec{a}$  is determined by

$$\vec{a} = -(\vec{v} \cdot \nabla) \vec{v} \quad (13)$$

And,  $d_p$  is the diameter of the nanoparticles of secondary phase  $s$  and  $\vec{a}$  is the secondary phase particle's acceleration,  $T_{nf}$  is the temperature,  $p$  is the pressure.

Also, the buoyancy term in the momentum equations (2) and (5) is approximated (Fluent [7]) by

$$(\rho - \rho_0)g \approx -\rho_0 \beta (T - T_0)g \quad (14)$$

which is considered when Boussinesq approximation is taken into account for mixed convection case. Here  $\beta$  is the thermal expansion coefficient of the fluid,  $\rho_0$  and  $T_0$  are the reference density and temperature respectively.

### Transitional Modelling:

Menter [10] developed the SST  $\kappa - \omega$  transitional model which is used here in the transitional modelling. The equations for the turbulence kinetic energy ( $\kappa$ ) and specific dissipation rate of turbulence kinetic energy ( $\omega$ ) used in the SST  $\kappa - \omega$  model are given with

$$\text{div}(\rho\kappa\vec{v}) = \text{div}\left\{\left(\mu + \frac{\mu_t}{\sigma_k}\right)\text{grad}\kappa\right\} + G_\kappa - \rho\kappa\omega\beta_1 \quad (15)$$

$$\begin{aligned} \text{div}(\rho\omega\vec{v}) = \text{div}\left\{\left(\mu + \frac{\mu_t}{\sigma_\omega}\right)\text{grad}\omega\right\} + G_\omega - \rho\omega^2\beta_2 \\ + 2(1 - F_1)\rho\sigma_{\omega,2} \frac{\text{grad}\omega\text{grad}\kappa}{\omega} \end{aligned} \quad (16)$$

In these equations,  $G_\kappa$  represents the generation of turbulence kinetic energy due to the mean velocity gradients,  $G_\omega$  represents the production of  $\omega$ , and  $\sigma_k$  and  $\sigma_\omega$  are the effective Prandtl numbers for the kinetic energy and specific rate of dissipation respectively. And turbulent viscosity  $\mu_{t,m}$  is modelled as

$$\mu_t = \frac{\rho\kappa}{\omega} \frac{1}{\max\left(\frac{1}{\alpha^*}, \frac{SF_2}{\alpha_1\omega}\right)} \quad (17)$$

Here,  $F_1$  and  $F_2$  are the blending functions,  $S$  is the strain rate magnitude and  $\alpha^*$  is a model constant. And, the model constants are  $\beta_1 = 0.075$ ,  $\beta_2 = 0.0828$ ,  $\alpha_1 = 0.31$ ,  $\sigma_k = 1.0$  and  $\sigma_\omega = 1.168$ . Further information of transitional modelling is available in Fluent [7].

### 3. Boundary Conditions

#### Single Phase model:

The following boundary conditions are used to solve the system of nonlinear partial differential equations (1-3).

At the pipe inlet, a uniform velocity ( $v_{x,in}$ ) as well as a uniform temperature ( $T_{in} = 293\text{ K}$ ) with a turbulent intensity ( $I = 3\%$ ) and hydraulic diameter ( $D_h = 0.019\text{ m}$ ) are stated. And, all the thermal properties used in this work are calculated at the inlet temperature ( $T_{in}$ ) that also is considered to be the reference temperature.

At the pipe outlet, a static gauge pressure,  $p_{gauge} = 0$ , is specified. And, the finite volume solver extrapolates the other flow and the scalar quantities such as the temperature and the turbulent quantities from the interior domain.

On the pipe wall, a no-slip boundary condition is introduced with uniform heat flux,  $q'' = 5000 \text{ W/m}^2$ .

### **Multi-phase model:**

The boundary conditions used in the single-phase model have been specified in the multi-phase mixture model for both the fluid and solid phases as well as for the mixture. Details of these boundary conditions are given below:

The velocity is specified for the fluid and nanoparticles phases at the pipe inlet where it is assumed that fluid and nanoparticles are flowing with the same local velocity. The nanoparticles concentrations for the nanoparticles phase is set too. And, turbulent intensity ( $I = 3\%$ ) and hydraulic diameter,  $D_h = 0.019 \text{ m}$ , as well as the inlet temperature ( $T = 293 \text{ K}$ ) are specified for the mixture.

However, no conditions are applied for the fluid and nanoparticles phases at the pipe outlet. Also, turbulent intensity ( $I = 3\%$ ) and hydraulic diameter,  $D_h = 0.019 \text{ m}$  are specified for the mixture.

No conditions are applied for the fluid and nanoparticles phases at the pipe wall too. And, a no-slip boundary condition as well as uniform heat flux ( $q'' = 5000 \text{ W/m}^2$ ) on the pipe wall are specified for the mixture.

Also, the Boussinesq approximation is introduced in the momentum equation for mixed convection nanofluids flow in the inclined pipe. Moreover, the details of nanofluids and base fluid (water) thermophysical properties are also described in Saha and Paul [1]. Also, details of numerical method also given in Saha and Paul [1].

## **4. Grid Sensitivity Analysis**

Grid sensitivity analysis has been carried out using different mesh volumes for the horizontal ( $\theta = 0^\circ$ ) and inclined ( $\theta = 45^\circ$ ) pipe orientations in order to achieve a suitable grid. The grid sensitivity results of radial velocity, temperature, turbulent kinetic energy and average Nusselt number with different mesh volumes for  $\text{Al}_2\text{O}_3\text{-H}_2\text{O}$  nanofluid are presented in Figs. 2 and 3.

Here, five different mesh control volumes considering a total element numbers of 274512, 275544, 294120, 462756 and 584022 have been considered respectively for a selected Reynolds number,  $Re$ , of 10000. The results of the radial velocity and temperature extracted

at the location of  $x = 0.99$  m where the flow fields seem to be fully developed shows insignificant variations along the radial direction with the mesh choices. However, a significant variation between the radial turbulent kinetic energy profiles is observed for a lower number of mesh volumes. But the results for the mesh volume of 462756 and 584022 are similar and so, 462756 are considered to be appropriate for the present investigation.

The variations of the average Nusselt number with different mesh volumes have also been presented in Fig. 3 in order to justify the final selection again. It clearly shows, in case of the mesh volume size being greater than 460000, any size of mesh volume can be adopted for nanofluids flow in pipe when the objective is to test the effect of inclination angles from  $0^\circ$  to  $75^\circ$ . It is significant that a uniform mesh distribution is considered along the pipe as well as the non-uniform mesh distributions are considered in other two directions in order to achieve better and accurate results of flow fields inside and near wall region of the pipe as shown in Fig. 4.

## 5. Results and Discussions

Here, Numerical investigations have been carried out using the  $\text{Al}_2\text{O}_3\text{-H}_2\text{O}$  and  $\text{TiO}_2\text{-H}_2\text{O}$  nanofluids with the following parameters: Reynolds number from  $Re = 2300$  to  $10 \times 10^3$  (transition regime), nanoparticles concentration,  $\chi = 6\%$ , diameter of nanoparticles,  $d_p = 10$  nm and pipe inclination angles from  $\theta = 0^\circ$  to  $75^\circ$ . At first, a comparison between the results of the 2D axi-symmetric (carried out in Saha and Paul [3]) and the 3D pipe model is presented in the following section. Then, velocity, temperature and turbulent kinetic energy contours are shown in order to understand the flow and thermal field behaviours. Later on, variation of the hydrodynamic and thermal critical distances as well as the Darcy friction factor and average Nusselt number with different inclination angles using the single and multi-phase models (SPM, MPM) are also presented and discussed.

### 5.1 Comparisons

Accuracy of the Darcy friction factor and average Nusselt number depend on the several factors such as good distribution of mesh along the axial; radial and tangential directions; choice of a transitional model; suitable boundary conditions near wall treatment as well as the physical geometry. Hence, it is important to compare the accuracy of the present results obtained in the 3D model geometry with some available experimental or numerical results. More essentially, comparison of the results obtained from the 2D axi-symmetric geometry

has been done to gain further confidence in the full 3D modelling. A horizontal pipe with two water based  $\text{Al}_2\text{O}_3$  and  $\text{TiO}_2$ nanofluids is considered to do this. Here, the chosen parameters are:  $Re = 2300$  to  $10000$ ,  $d_p = 10 \text{ nm}$ ,  $\chi = 6\%$  with the Brownian motion of nanoparticles.

Figure 5 shows the variations of the Darcy friction factor and average Nusselt number with different Reynolds numbers. It is observed that for the  $\text{Al}_2\text{O}_3$ - $\text{H}_2\text{O}$  nanofluid, the maximum percentages of variations among the results of average Nusselt number obtained from the 2D axi-symmetric model are 3.12% and 4.27% respectively with the single and multi-phase models. However, such variations are found to be 4.06% and 4.98% respectively for the  $\text{TiO}_2$ - $\text{H}_2\text{O}$  nanofluid. The maximum percentage of variations among the results of Darcy friction factor is found to be less than 1%. And, there is no significant difference found between the Darcy friction factor results while using the single and multi-phase models. Since the goal is to justify the accuracy of the simulated results of 3D model, Figure 5 shows a strong agreement compared with the results obtained using the 2D axi-symmetric model that have already been presented, verified and described in Saha and Paul [3].

## 5.2 Velocity Contours

In this section, 2D contour plots of velocity have been generated by placing a horizontal plane along the pipe and also at different axial positions in order to understand the flow field behaviour in details for different inclination angles as shown in Fig. 6. Only  $\text{Al}_2\text{O}_3$ - $\text{H}_2\text{O}$  nanofluid with single phase model has been selected and the Reynolds number has been fixed to  $Re = 3500$ .

The transition phenomena observed previously in the axisymmetric model (Saha and Paul [3]) remains to be the same in case of  $\theta = 0^\circ$ . For example, the axial velocity initially behaves like a laminar flow and the transition begins at the hydrodynamic critical point. At this point, the hydrodynamic boundary layer thickness starts to grow and such development is found higher than the boundary layer growth observed in the upstream region. After the laminar breakdown point, the development of hydrodynamic boundary layer tends to become constant suggesting the flow to be fully developed. However, the development of a pair of unequal cells near the upstream at the top and bottom walls of the pipe is observed when the inclination angle is increased e.g. for  $\theta = 0^\circ$  to  $30^\circ$ . The upper one forms a larger size cell with a higher velocity magnitude than the lower one. It is also noticed that the development of lower sized cell is weak while the upper sized cell is stronger which dominates the flow at

the upstream region. Also, the development of these two cells is seen to be limited within the region  $L < 0.3 \text{ m}$  and this may be due to the buoyancy force which comes into effect due to the inclination angle. Besides, the flow starts to be fully developed further from the upstream and also in the downstream regions. And, such development is found to be identical because of the symmetry.

As the inclination angle is further increased from  $\theta = 30^\circ$  to  $75^\circ$ , the larger size cell starts to reduce but the smaller size cell starts to enhance. Similarly, the development area of these two cells decreases and is found to be less than  $0.2 \text{ m}$ . Moreover, as the lower cell moves towards the centreline region of the pipe, such rapid expansion forces the upper cell to reduce its size as which is clearly visible in frames (e, f). Since the lower cell becomes dominate in the pipe affecting the growth of the upper cell, it suggests that the upper cell is going to be diminished with the further increase of the inclination angle.

Moreover, Fig. 7 shows the variations of the velocity contours at different axial positions with different inclination angles. In case of  $\theta = 15^\circ$  and at  $x = 0.1 \text{ m}$ , it is observed that the higher velocity region tends to move towards the upper wall zone and forms a large size of cell with lower velocity region that is likely to cover lower wall zone. Whereas for  $\theta = 30^\circ$  and  $x = 0.1 \text{ m}$ , a rapid decrease of higher velocity region which tends to move more towards the upper wall region is observed and the large size of cell forms a quarter moon type profile. Also, a small development of lower velocity zone seems to grow near the lower wall region. A degeneration of higher velocity region and moon type profile are seen near the top wall of the pipe and a rapid development of lower velocity region is observed for  $\theta = 45^\circ$  to  $60^\circ$  and  $x = 0.1 \text{ m}$ . Though for  $\theta = 75^\circ$  and  $x = 0.1 \text{ m}$ , a higher velocity cell seems to diminish and the whole region is almost covered with the lower velocity fluid. Again, it is observed that the higher velocity cell moves towards the upper wall region and forms a semi-circular profile while other regions are covered with the lower velocity magnitude of the nanofluid in case of  $\theta = 15^\circ$  to  $30^\circ$  and  $x = 0.25 \text{ m}$ . However, for  $\theta = 45^\circ$  to  $75^\circ$  and  $x = 0.25 \text{ m}$ , higher velocity region seems to diminish and the lower velocity fluid tends to cover the whole region. When  $x > 0.25 \text{ m}$ , the flow tends to be fully developed and decrease of velocity magnitude is observed with the increase of inclination angles.

### **5.3 Turbulent Kinetic Energy Contours**

Figures 8 and 9 show the variations of turbulent kinetic energy along the pipe with different inclination angles using single phase model for  $\text{Al}_2\text{O}_3\text{-H}_2\text{O}$  nanofluid. For  $\theta = 0^\circ$ , the initial

blue region near the upstream indicates that the turbulent kinetic energy is almost constant and the flow behaviour seems to be laminar. This agrees well with the results reported in Saha and Paul [3].

When  $L > 0.2 m$ , the turbulent kinetic energy starts to develop and a rapid increase is observed at the laminar breakdown point near the wall region. Though the laminar behaviour at the upstream tends to disappear and development of a large cell near the lower region of the pipe wall is observed for  $\theta = 15^\circ$  to  $30^\circ$ . Also, a small glimpse of the growth of higher magnitude of turbulent kinetic energy cell is visible inside the large and developed cell near the centreline position of the upstream. When  $0.2 m < L < 0.4 m$ , the large cell is seen to cover almost the centreline area. And, another development of small cell which is connected to the large cell is evident near the upper wall. Besides, both the cells start to decrease when  $L > 0.4 m$ . Moreover, the growth of boundary layer start to be steady, constant and identical along the pipe at the downstream because of the symmetry boundary conditions and as the flow tends to be fully developed.

As the inclination angle increases from  $\theta = 30^\circ$  to  $75^\circ$ , the large cell starts to be reduced in size as well as the growth of higher magnitude of turbulent kinetic energy inside the large cell starts to increase rapidly at the same time. Also, the development area of the large cell is decreased and is found to be less than  $0.3 m$ . Moreover, the higher magnitude cell lying inside the large cell moves towards the centreline region and such augmentation forces the small cell located near the upper wall to be reduced. This is clearly visible in Figs. 8 and 9. As the inclination angle increases, the combination of higher magnitude cell and the large cell forms a womb like profile which is reduced with the increase of inclination angles.

#### **5.4 Temperature Contours**

In this section, variations of the temperature profile along the pipe for different inclination angles has been presented in Figs. 10 and 11 to understand how the Buoyancy force affects the thermal field as well.

For  $\theta = 0^\circ$ , it is found that most of the region of the pipe is covered with the deep blue colour that refers to the lower temperature region. On the other hand, higher temperature is observed near the wall region. Also, the maximum temperature difference between the higher and lower temperature region is found to be approximately  $6K$ . Moreover, the growth of thermal boundary layer seems to be steady and fully developed when  $x > 0.25 m$ . Again, it is worth

noting that these behaviours agree well with the previous findings reported in Saha and Paul [3].

For  $\theta = 15^\circ$ , a sudden change in the growth of thermal boundary layer is observed near the bottom wall region when  $x < 0.2 \text{ m}$ . But after that region, a development of boundary layer seems to be steady and tends to be fully developed. Similar behaviour is also observed for  $\theta = 30^\circ$  and  $45^\circ$ . This behaviour indicates the effect of the Buoyancy force when the Boussinesq approximation is considered. For  $\theta = 60^\circ$  and  $75^\circ$ , a deformation of the growth of thermal boundary layer is observed near the top wall when  $x < 0.2 \text{ m}$ . However, the development of boundary layer seems to be more pronounced and higher boundary layer thickness is also observed for the increase of inclination angles when  $x > 0.2 \text{ m}$  for the increase of inclination angles. This suggests, the thermal flow field tends to behave more like a fully developed turbulent flow than that of transition flow.

In particular, the thermal critical distance decreases and moves towards the upstream region with the increase of inclination angles from  $\theta = 0^\circ$  to  $45^\circ$  for  $\text{Al}_2\text{O}_3\text{-H}_2\text{O}$  nanofluid. It suggests that the transition behaviour of the thermal field starts to diminish due to the buoyancy force for the higher inclined pipe. Again, the existence of thermal critical point is not visible for  $\theta = 60^\circ$ . This suggests that the buoyancy force plays a dominant role in the mixed convection and transition behaviour of thermal field tends to vanish. On the other hand, the surface temperature starts to rise initially for  $\theta = 75^\circ$  though it suddenly decreases then. And it starts to rise rapidly again. This behaviour indicates, there is a quick transformation of surface temperature from transition to turbulent regime. Although such behaviour follows neither the transition nor the turbulent behaviours fully, results suggest that turbulence is more dominance in the flow and thermal fields. This can be justified further from Figs. 8 and 9 since the maximum turbulent kinetic energy found here is  $0.01121 \text{ m}^2/\text{s}^2$ ,  $0.014022 \text{ m}^2/\text{s}^2$ ,  $0.02085 \text{ m}^2/\text{s}^2$ ,  $0.024193 \text{ m}^2/\text{s}^2$ ,  $0.024605 \text{ m}^2/\text{s}^2$  and  $0.024665 \text{ m}^2/\text{s}^2$  for  $\theta = 0^\circ$ ,  $15^\circ$ ,  $30^\circ$ ,  $45^\circ$ ,  $60^\circ$  and  $75^\circ$  respectively.

## 5.5 Critical Distance

A detailed investigation has been carried out in order to understand the behaviour of hydrodynamic and thermal critical distances and the results are presented in Fig. 9.12. Here, both the hydrodynamic and thermal critical distances decrease with the increase of inclination angles though no transition behaviour of the thermal flow field is observed for  $\theta \geq 60^\circ$ . This is already shown in Fig. 10. It indicates, the transition behaviour of thermal flow field is more

affected by the Buoyancy force in the mixed convection. Two different peak positions clearly visible in Figs. 10 and 11 is found to be present when  $\theta > 60^\circ$ . These positions can be referred to the first and second transition points respectively. Another investigation has been carried out to understand the behaviour of thermal critical distance for  $\theta \geq 60^\circ$  and the results are presented in Fig. 13. Here, the first and second critical distances decrease with the increase of inclination angles when  $\theta > 60^\circ$ . It is also observed that the first critical distance decreases with the increase of Reynolds number when  $Re < 4000$ . But, such distance becomes constant when  $4000 \leq Re \leq 10000$ . The second critical distance decreases with the increase of Reynolds number when  $Re < 8000$  and then it becomes constant when  $8000 \leq Re \leq 10000$ . Such behaviour indicates that the way of flow separation and critical distances are quite different when  $\theta \geq 60^\circ$ . Also, the flow separation causes more disturbances in the flow field and the separated flow tends to behave like more turbulent than transition due to the Buoyancy force.

Another particular investigation is done to understand the variations of maximum turbulent kinetic energy with different Reynolds number for different inclination angles as shown in Fig. 14. It is observed that the maximum turbulent kinetic energy increases with the increase of inclination angles when  $\theta < 60^\circ$ . But it starts to decrease with the increase of inclination angles when  $\theta \geq 60^\circ$ . Such behaviour supports the findings shown in Figs. 10 to 13. As it has been already discussed, the transition behaviour tends to diminish when  $0^\circ \leq \theta < 60^\circ$  and both the local  $Nu$  and surface temperature  $T$  behave like neither fully transition nor fully turbulent flow when  $\theta \geq 60^\circ$ . Such changes in behaviour are also visible in the results shown in Fig. 14. The hydrodynamic and thermal critical distances are strongly dependent on the Reynolds number as well as on the inclination angle but independent to the types of nanofluids, nanoparticles diameters and concentrations. These findings are realistic and physically valid with what has been shown in Saha and Paul [3].

## 5.6 Darcy Friction Factor Behaviour

Darcy friction factor results are presented in Fig. 15 with a view to understand the pressure drop behaviour affected by the Buoyancy force inside the inclined pipe. To do this, the variations of Darcy friction factor with different inclination angles and the Reynolds numbers for  $Al_2O_3-H_2O$  and  $TiO_2-H_2O$  nanofluids have been presented here. There is an insignificant difference between the Darcy friction factor results of nanofluids and water in the horizontal pipe. This has been described in Saha and Paul [3]. But, the Darcy friction factor increases

with the increase of inclination angle from  $\theta = 0^\circ$  to  $75^\circ$  in the inclined pipe. Also, a higher Darcy friction factor is observed in the mixed convection case than that is seen in the forced convection. It is the additional buoyant force which compels to enhance the pressure drop inside the pipe. Again, more significant enhancement of Darcy friction factor in the mixed convection case is observed than that found in the forced convection case for low Reynolds number and  $\theta = 30^\circ$ . As the inclination angle increases, such rapid enhancement tends to reduce in comparison with the Darcy friction factor result of  $\theta = 30^\circ$ . This is again the buoyancy force which affects the flow and pressure fields. In addition, there have been insignificant differences among the Darcy friction factor results with different inclination angles while using both  $\text{Al}_2\text{O}_3\text{-H}_2\text{O}$  and  $\text{TiO}_2\text{-H}_2\text{O}$  nanofluids for the higher Reynolds number such as  $Re \geq 8000$ .

In the particular cases for  $\text{Al}_2\text{O}_3\text{-H}_2\text{O}$  nanofluid, the maximum percentages of the variations of Darcy friction factor are 12.86%, 22.13%, 29.41% and 32.80% respectively compared with the Darcy friction factor results in horizontal pipe with the inclination angles of  $30^\circ$ ,  $45^\circ$ ,  $60^\circ$  and  $75^\circ$ . However, the maximum percentages of the variations of Darcy friction factor are found to be 12.81%, 21.64%, 29.49% and 32.97% respectively in such cases of  $\text{TiO}_2\text{-H}_2\text{O}$  nanofluid with the inclination angles of  $30^\circ$ ,  $45^\circ$ ,  $60^\circ$  and  $75^\circ$ . These reveal,  $\text{Al}_2\text{O}_3\text{-H}_2\text{O}$  nanofluid shows the higher percentages of enhancement in Darcy friction factor than  $\text{TiO}_2\text{-H}_2\text{O}$  nanofluid for  $\theta = 30^\circ$  and  $45^\circ$ . Though, the opposite trend is observed in case of  $\theta = 60^\circ$  and  $75^\circ$ . Besides, the maximum percentages of the enhancement in Darcy friction factor is observed for  $\theta = 75^\circ$  while using  $\text{TiO}_2\text{-H}_2\text{O}$  nanofluid.

## 5.7 Average Nusselt Number Behaviour

Figure 16 shows the variations of average Nusselt number with the Reynolds number and different inclination angles from  $\theta = 0^\circ$  to  $75^\circ$  for  $\text{Al}_2\text{O}_3\text{-water}$  and  $\text{TiO}_2\text{-water}$  nanofluids. Here, both the single phase model (SPM) and multi-phase model (MPM) are considered. At this point, the average Nusselt number is observed to decrease with the increase of inclination angles from  $\theta = 0^\circ$  to  $75^\circ$  and the higher average Nusselt number is found in the multi-phase model than in the single phase model. Also, the average Nusselt number of the nanofluids is always higher than that of water at any given Reynolds number for  $\theta = 0^\circ$  to  $75^\circ$ .

In particular, the maximum percentages of deviation are approximately 3.87%, 10.05%, 16.32% and 19.48% respectively for  $\text{Al}_2\text{O}_3\text{-H}_2\text{O}$  nanofluid, single phase model and  $\theta = 30^\circ$ ,  $45^\circ$ ,  $60^\circ$  and  $75^\circ$ . These are lower than that in the horizontal pipe. While for multi-phase

model, these are approximately 3.81%, 9.89%, 16.21% and 19.31% respectively and lower than that in the horizontal pipe too. However, the maximum percentages of deviation are approximately 4.34%, 9.18%, 14.90% and 18.71% respectively for  $\text{TiO}_2\text{-H}_2\text{O}$  nanofluid, single phase model and  $\theta = 30^\circ, 45^\circ, 60^\circ$  and  $75^\circ$ . Similarly, these are approximately 4.28%, 9.02%, 14.76% and 18.58% respectively for multi-phase model. All of these percentages are lower than those in the horizontal pipe. These results indicate, the average Nusselt number in inclined pipes are lower than that of horizontal pipe and the maximum degeneration of heat transfer is observed for  $\theta = 75^\circ$  and  $\text{Al}_2\text{O}_3\text{-H}_2\text{O}$  nanofluid. The reason behind such degeneration of heat transfer rate in inclined pipe is the effect of buoyancy. Because, it forces to enhance the surface wall temperature resulting the reduction of heat transfer rate in comparison with the heat transfer rate in horizontal pipe.

## 6. Conclusion

Numerical investigation has been performed in order to understand the heat transfer behaviour of transition mixed convection in inclined pipe. And, two different types of nanofluids such as  $\text{Al}_2\text{O}_3\text{-water}$  and  $\text{TiO}_2\text{-water}$  nanofluids have been considered as working fluid as well as two different models called the single and multi-phase models have been used throughout this investigation. Results are presented in terms of velocity, temperature and turbulent kinetic energy contours, critical distance and average Nusselt number as well as Darcy friction factor. The following conclusions can be drawn from the outcomes:

- The contours of flow field and turbulent kinetic energy are found to be distorted near the upstream region along with the increase of inclination angles due to Buoyancy force.
- The surface temperature is observed to increase along with the increase of Reynolds number in the different inclination angles. Also, higher surface temperature is observed for the higher inclination angles. Such enhancement of wall temperature is responsible for the degeneration of heat transfer rate.
- The Darcy friction factor is increased along with the increase of Reynolds number in different inclination angles. Also, the higher Darcy friction factor is noticed in the higher inclination angles. And, such enhancement is found to be liable for the higher penalty in pumping power.

- The local Nusselt number is decreased with the increase of inclination angles. Also, it is found that transition behaviour of local Nusselt number exists for  $0^\circ < \theta < 55^\circ$  and then it starts to diminish. And then, neither transition nor turbulent behaviour is seen when  $\theta > 60^\circ$ .
- The average heat transfer rate is decreased along with the increase of Reynolds number in different inclination angles. It suggests, mixed convection has opposite effect on the inclined pipe than the forced convection on the horizontal pipe.

### **Acknowledgement**

The first author acknowledges the receipt of a studentship from the College of Science and Engineering and a SORSAS award.

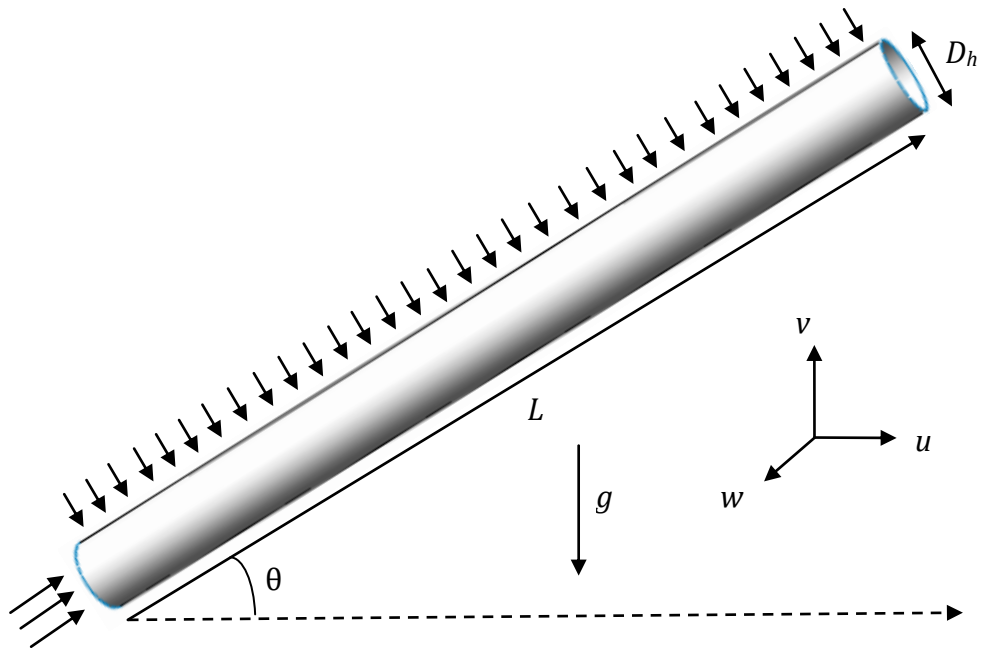


Figure 1: Schematic diagram of the geometry under consideration

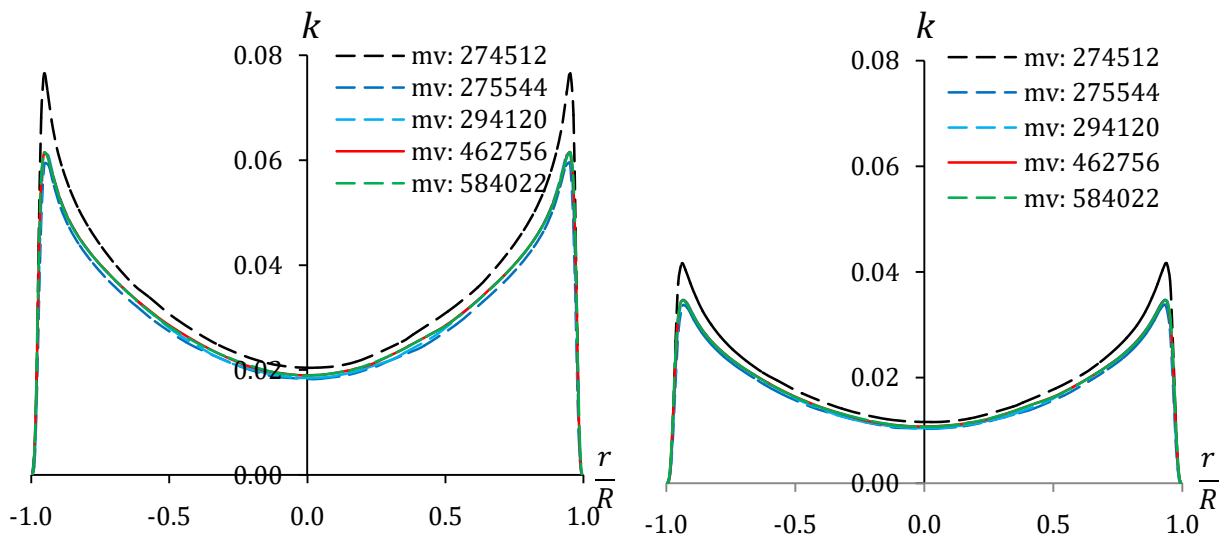
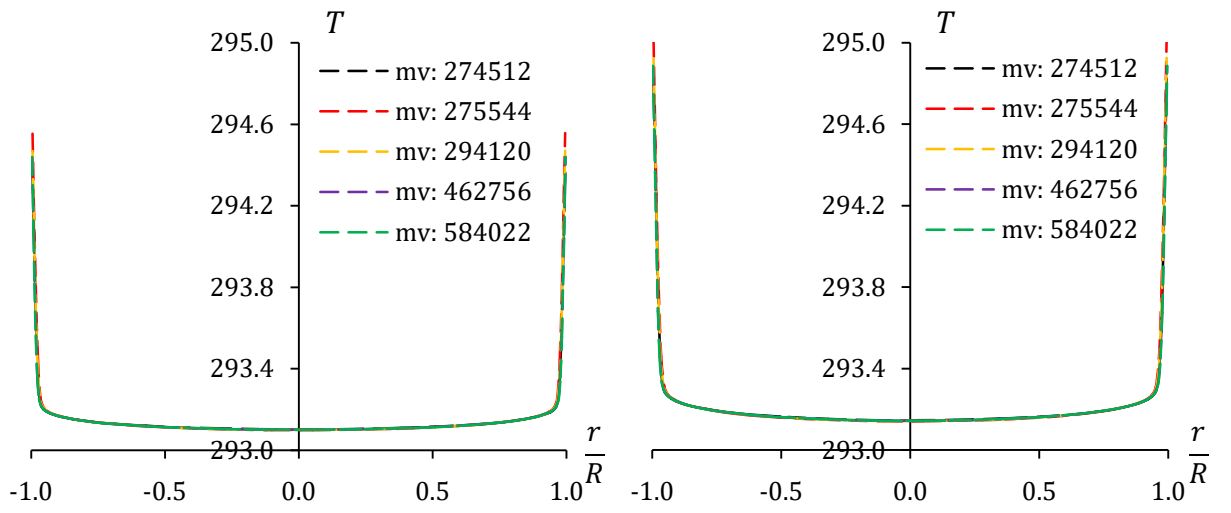
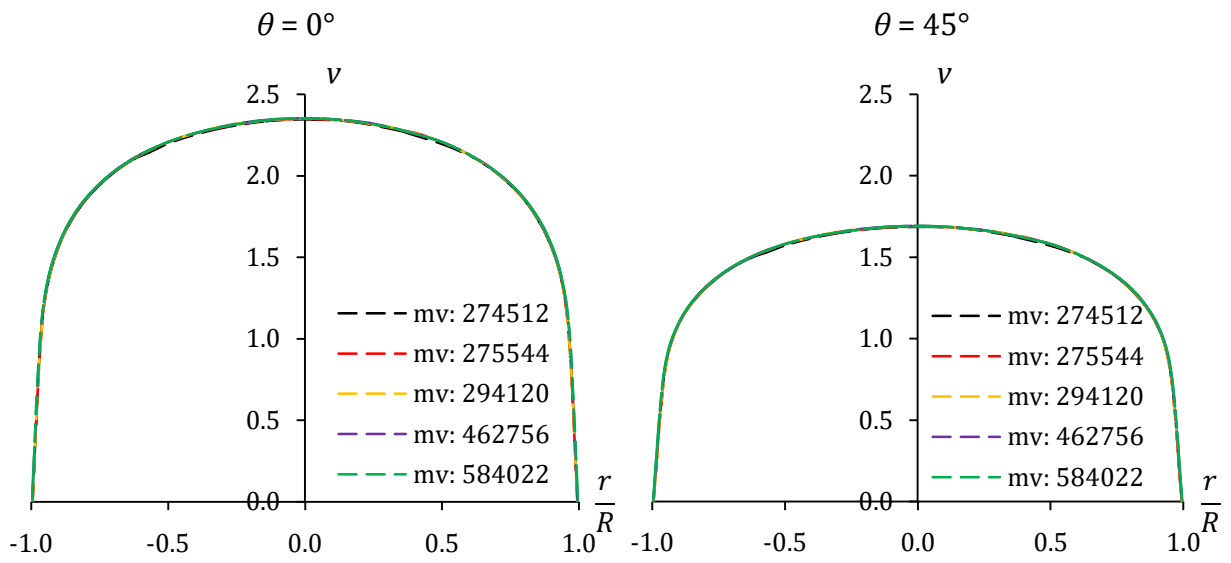


Figure 2: Variations of radial velocity, temperature and turbulent kinetic energy at  $x = 0.99\text{ m}$  with different mesh volumes for  $Re = 10000$ ,  $\theta = 0^\circ$  and  $\theta = 45^\circ$ , and  $\text{Al}_2\text{O}_3\text{-H}_2\text{O}$  nanofluid ( $mv$  refers to mesh volume)

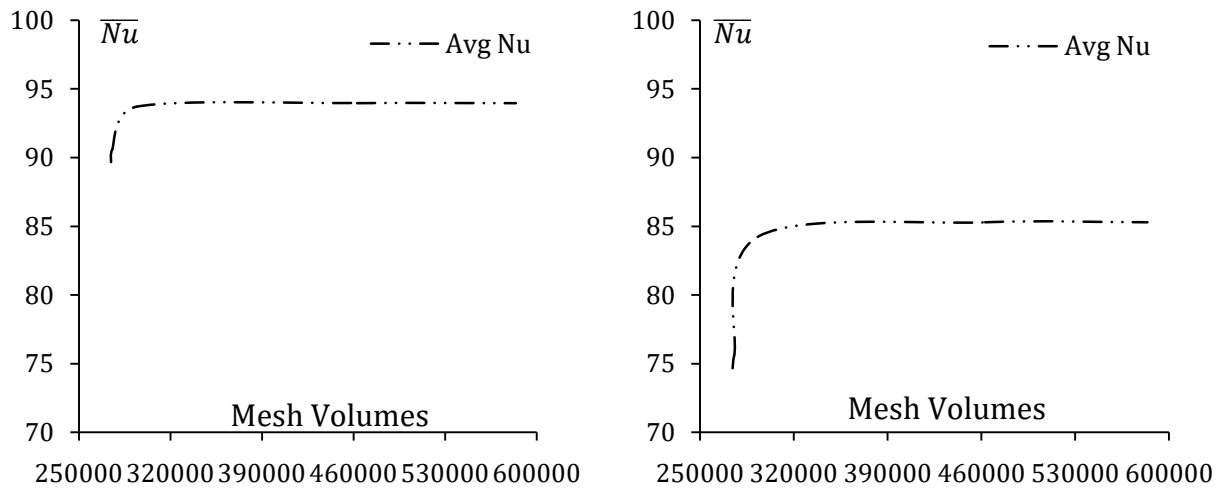


Figure 3: Variations of average Nusselt number with different mesh volumes for  $Re = 10000$ ,  $\theta = 0^\circ$  and  $\theta = 45^\circ$ , and  $\text{Al}_2\text{O}_3\text{-H}_2\text{O}$  nanofluid

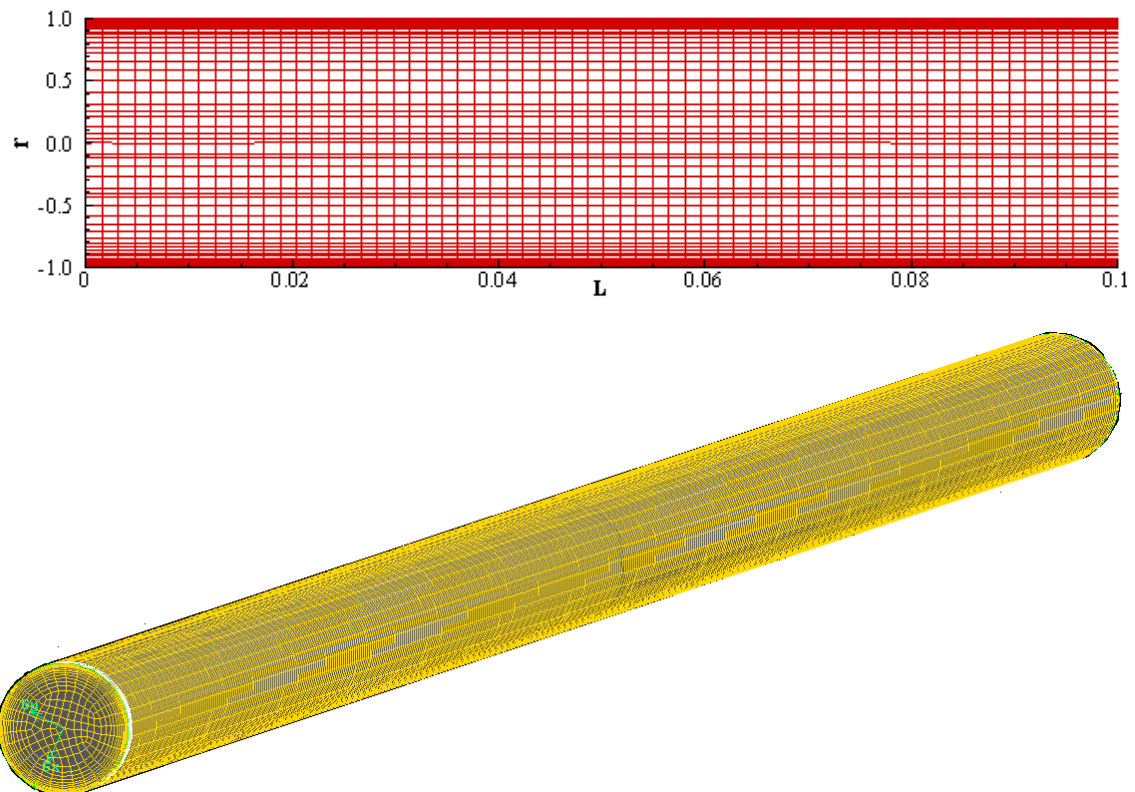


Figure 4: 2D and 3D view of mesh distributions along the pipe

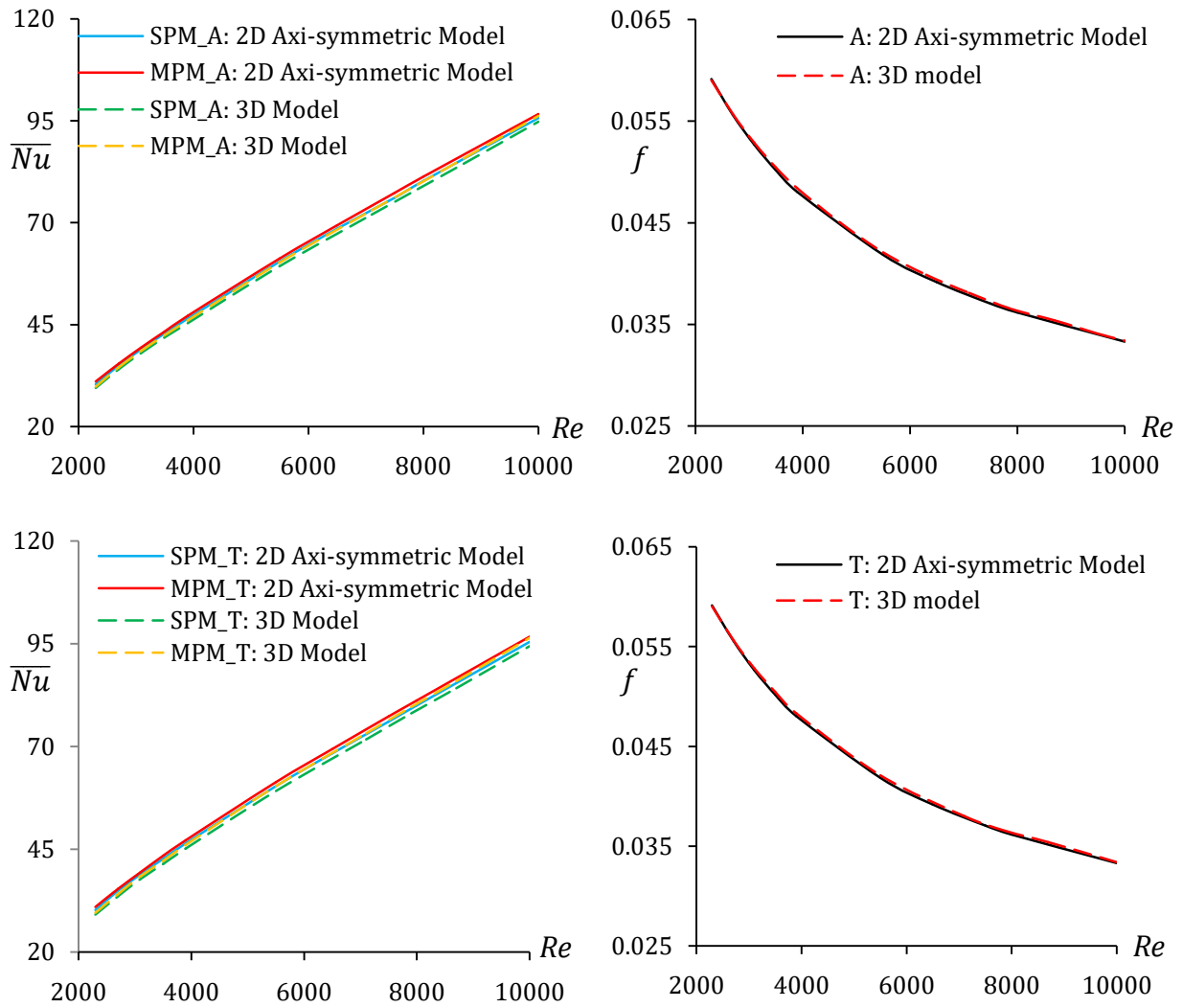


Figure 5: Comparisons between the results of average Nusselt number and Darcy friction factor of horizontal pipe with different Reynolds numbers using the 2D axi-symmetric and 3D models for A: Al<sub>2</sub>O<sub>3</sub>-H<sub>2</sub>O and T: TiO<sub>2</sub>-H<sub>2</sub>O nanofluids

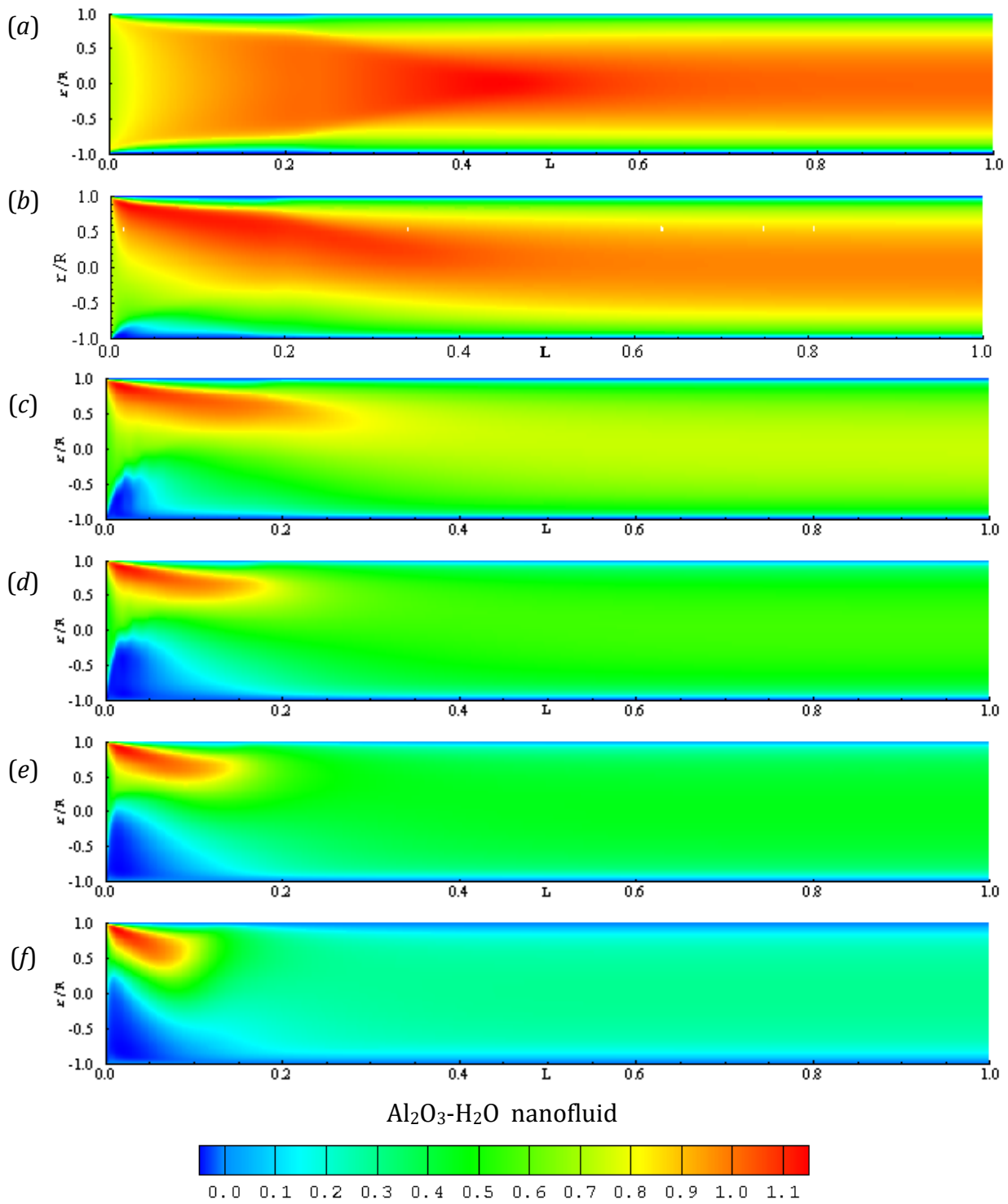


Figure 6: Variations of axial velocity along the pipe for different inclination angles (a)  $\theta = 0^\circ$ , (b)  $\theta = 15^\circ$ , (c)  $\theta = 30^\circ$ , (d)  $\theta = 45^\circ$ , (e)  $\theta = 60^\circ$ , (f)  $\theta = 75^\circ$  and  $Re = 3500$

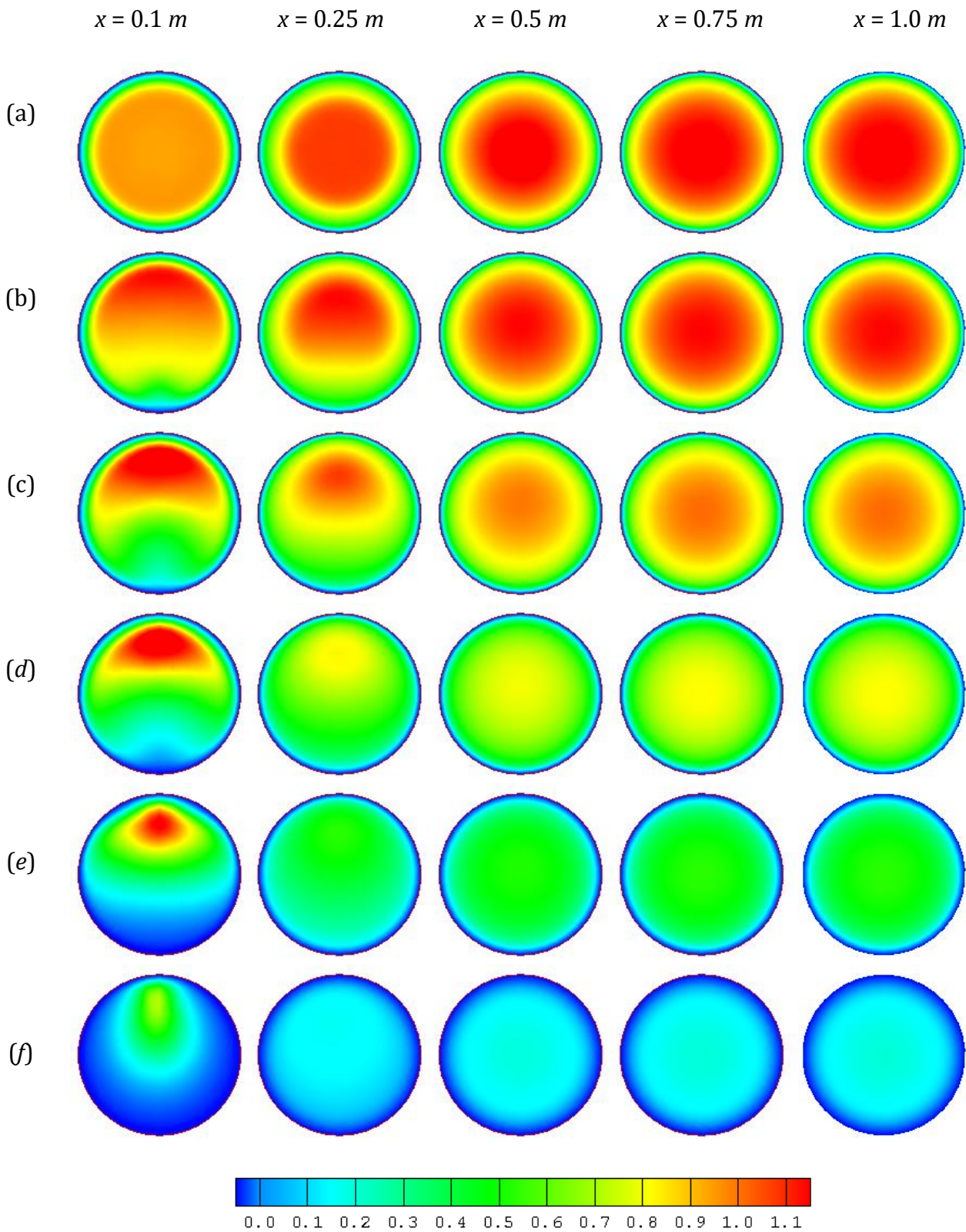


Figure 7: Velocity contours for different inclination angles (a)  $\theta = 0^\circ$ , (b)  $\theta = 15^\circ$ , (c)  $\theta = 30^\circ$ , (d)  $\theta = 45^\circ$ , (e)  $\theta = 60^\circ$ , (f)  $\theta = 75^\circ$  and  $Re = 3500$  at axial position  $x = 0.1 m$ ,  $0.25 m$ ,  $0.5 m$ ,  $0.75 m$  and  $1.0 m$ (left to right) respectively.

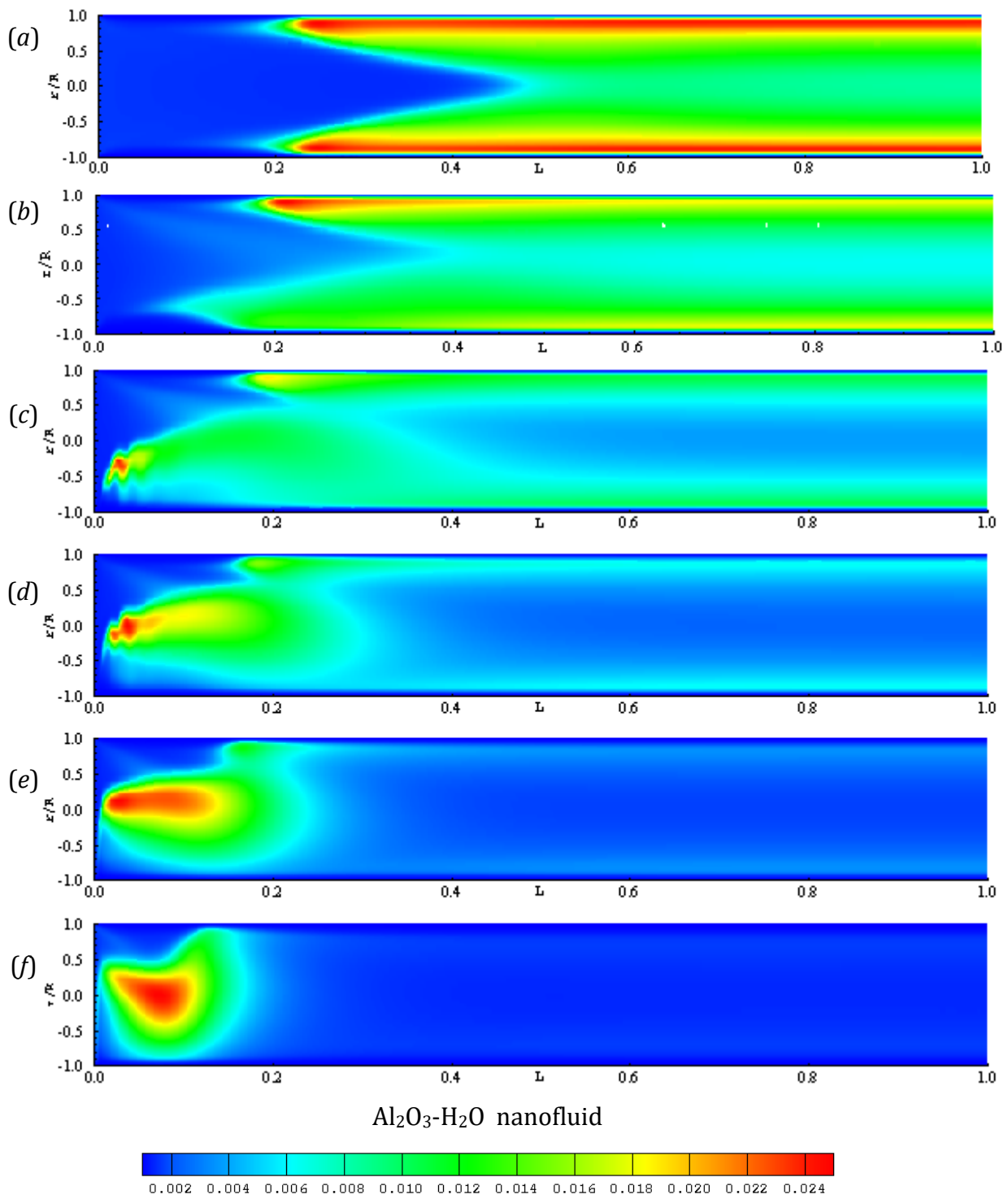


Figure 8: Variations of turbulent kinetic energy along the pipe for different inclination angles (a)  $\theta = 0^\circ$ , (b)  $\theta = 15^\circ$ , (c)  $\theta = 30^\circ$ , (d)  $\theta = 45^\circ$ , (e)  $\theta = 60^\circ$ , (f)  $\theta = 75^\circ$  and  $Re = 3500$

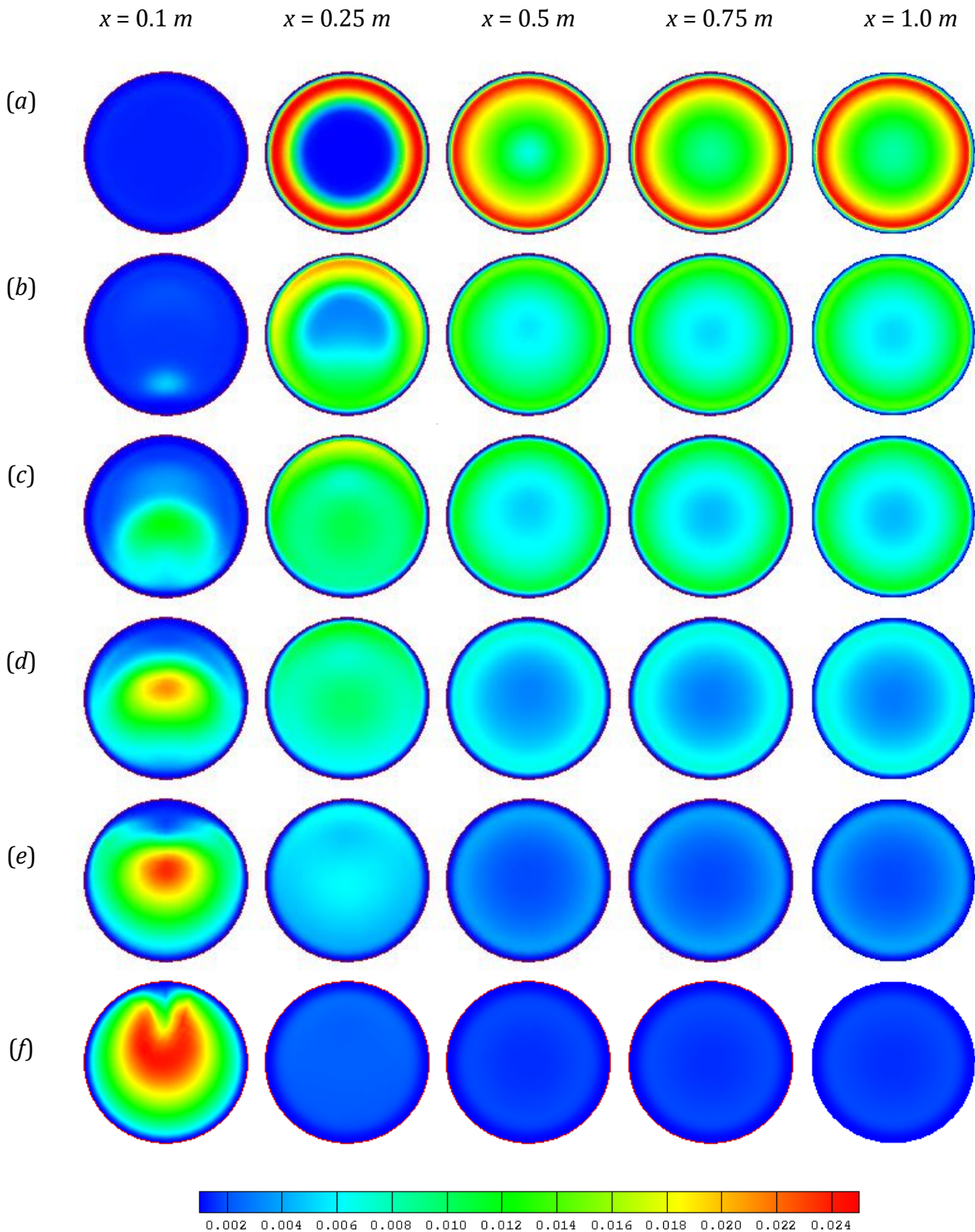


Figure 9: Turbulent kinetic energy contours for different inclination angles (a)  $\theta = 0^\circ$ , (b)  $\theta = 15^\circ$ , (c)  $\theta = 30^\circ$ , (d)  $\theta = 45^\circ$ , (e)  $\theta = 60^\circ$ , (f)  $\theta = 75^\circ$  and  $Re = 3500$  at axial position  $x = 0.1\text{ m}$ ,  $0.25\text{ m}$ ,  $0.5\text{ m}$ ,  $0.75\text{ m}$  and  $1.0\text{ m}$  respectively

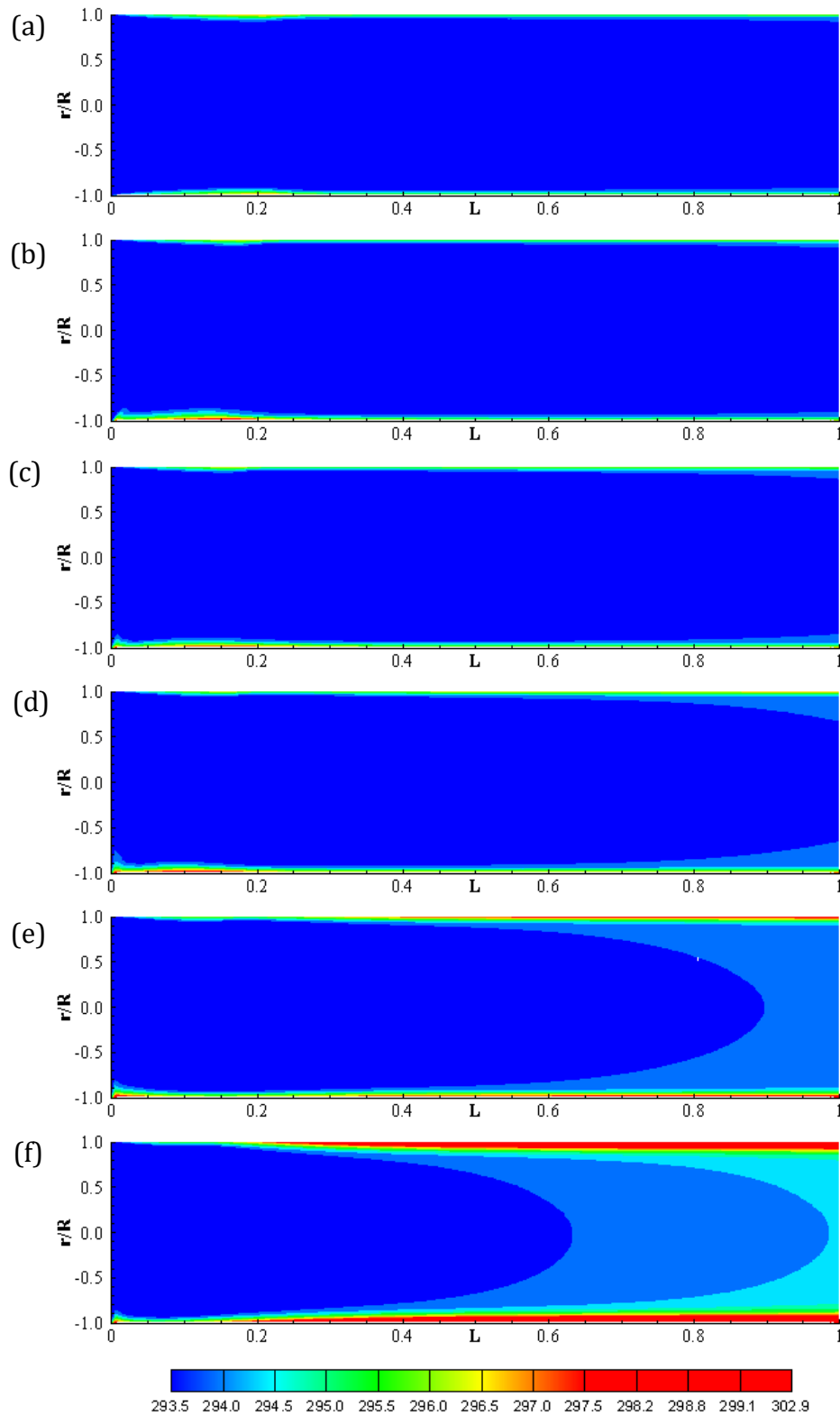


Figure 10: Variations of temperature along the pipe for different inclination angles (a)  $\theta = 0^\circ$ , (b)  $\theta = 15^\circ$ , (c)  $\theta = 30^\circ$ , (d)  $\theta = 45^\circ$ , (e)  $\theta = 60^\circ$ , (f)  $\theta = 75^\circ$  and  $Re = 3500$

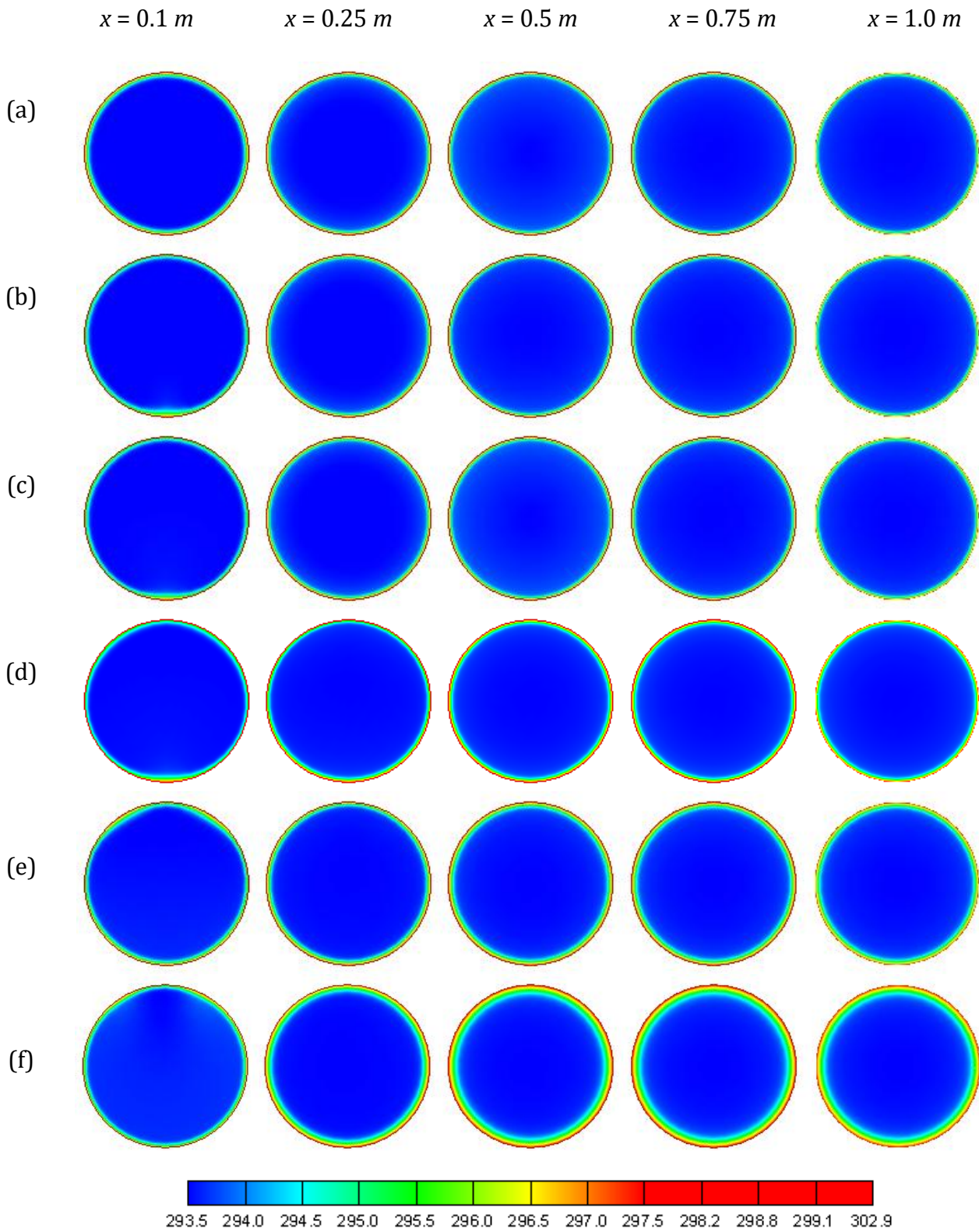


Figure 11: Temperature contours for different inclination angles (a)  $\theta = 0^\circ$ , (b)  $\theta = 15^\circ$ , (c)  $\theta = 30^\circ$ , (d)  $\theta = 45^\circ$ , (e)  $\theta = 60^\circ$ , (f)  $\theta = 75^\circ$  and  $Re = 3500$  at axial position  $x = 0.1 \text{ m}$ ,  $0.25 \text{ m}$ ,  $0.5 \text{ m}$ ,  $0.75 \text{ m}$  and  $1.0 \text{ m}$  respectively

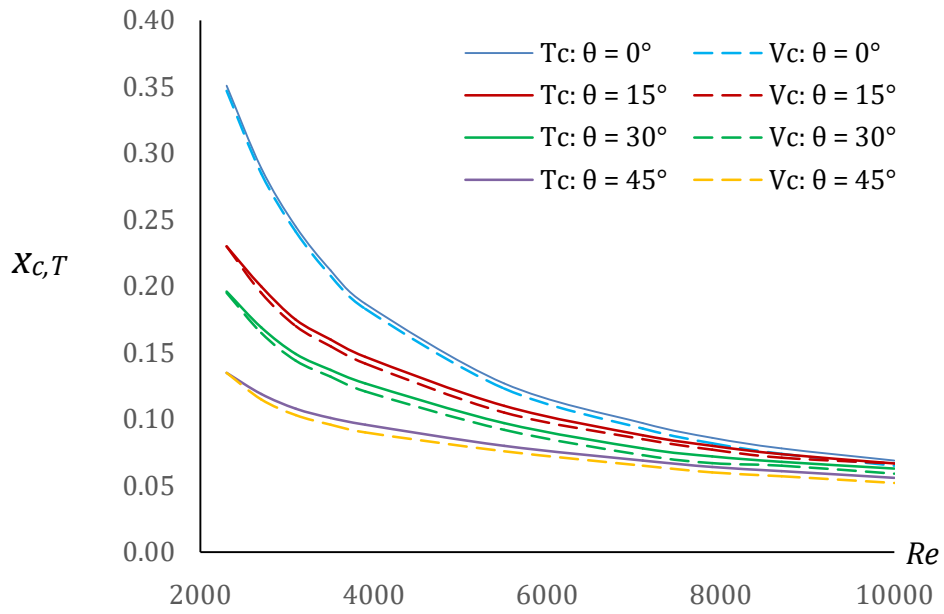


Figure 12: Variations of thermal and hydrodynamic critical distances with different Reynolds numbers for different inclination angles,  $\theta = 0^\circ$  to  $45^\circ$

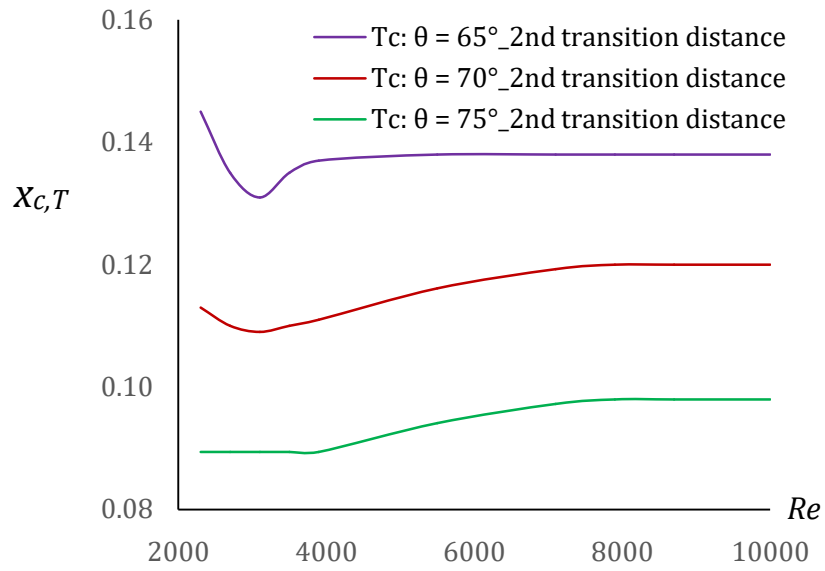
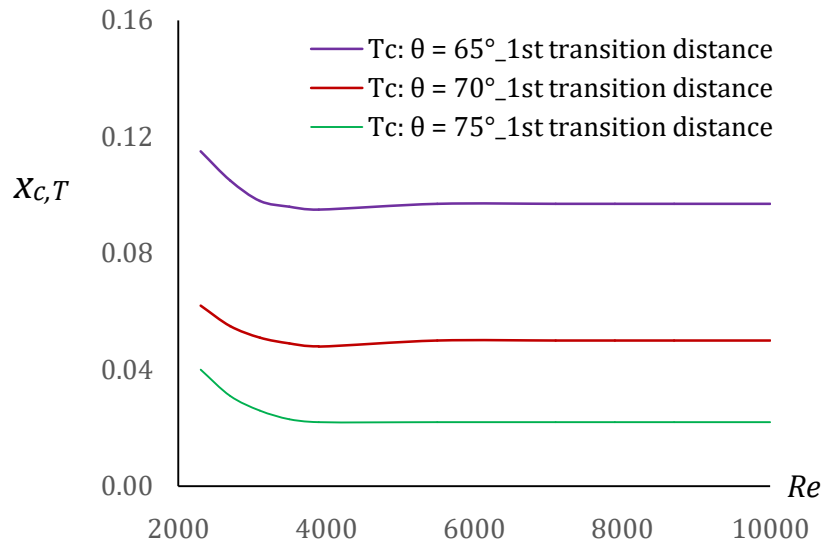


Figure 13: Variations of thermal critical distances with different Reynolds numbers for different inclination angles,  $\theta = 65^\circ$  to  $75^\circ$

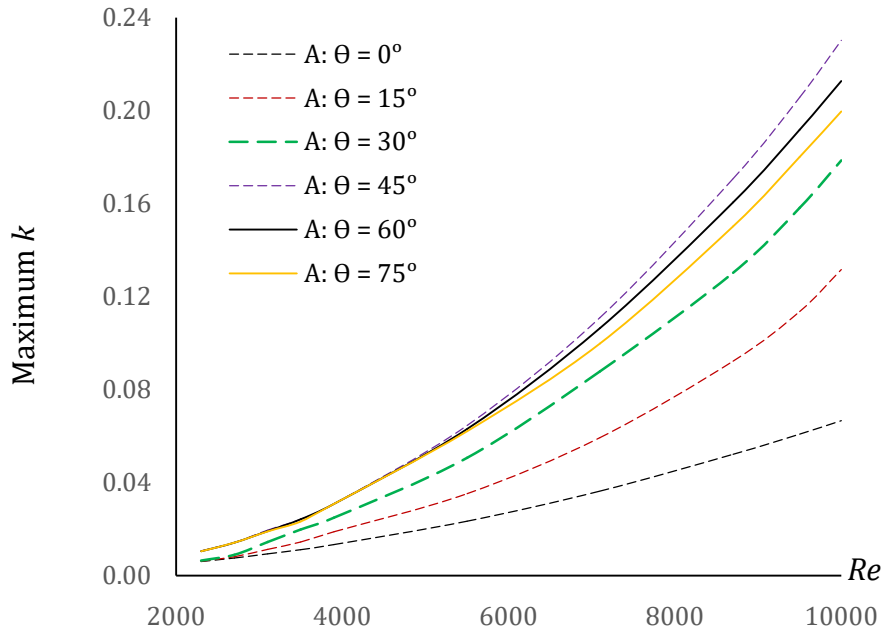


Figure 14: Variations of maximum turbulent kinetic energy ( $k$ ) with Reynolds numbers for different inclination angles,  $\theta = 0^\circ$  to  $75^\circ$

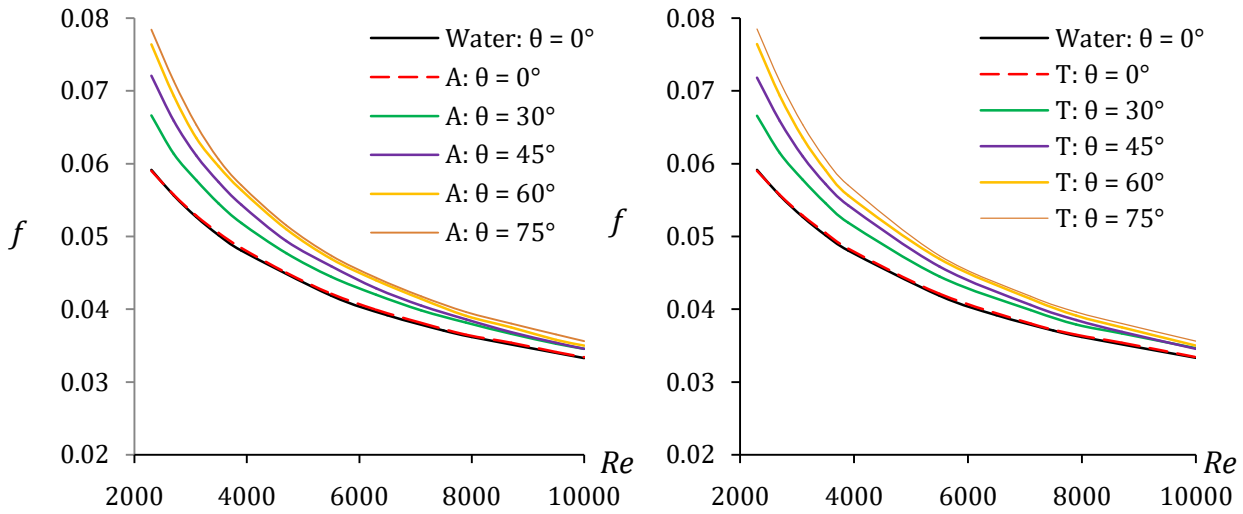


Figure 15: Variations of Darcy friction factor with different Reynolds numbers for different inclination angles,  $\theta = 0^\circ$  to  $75^\circ$

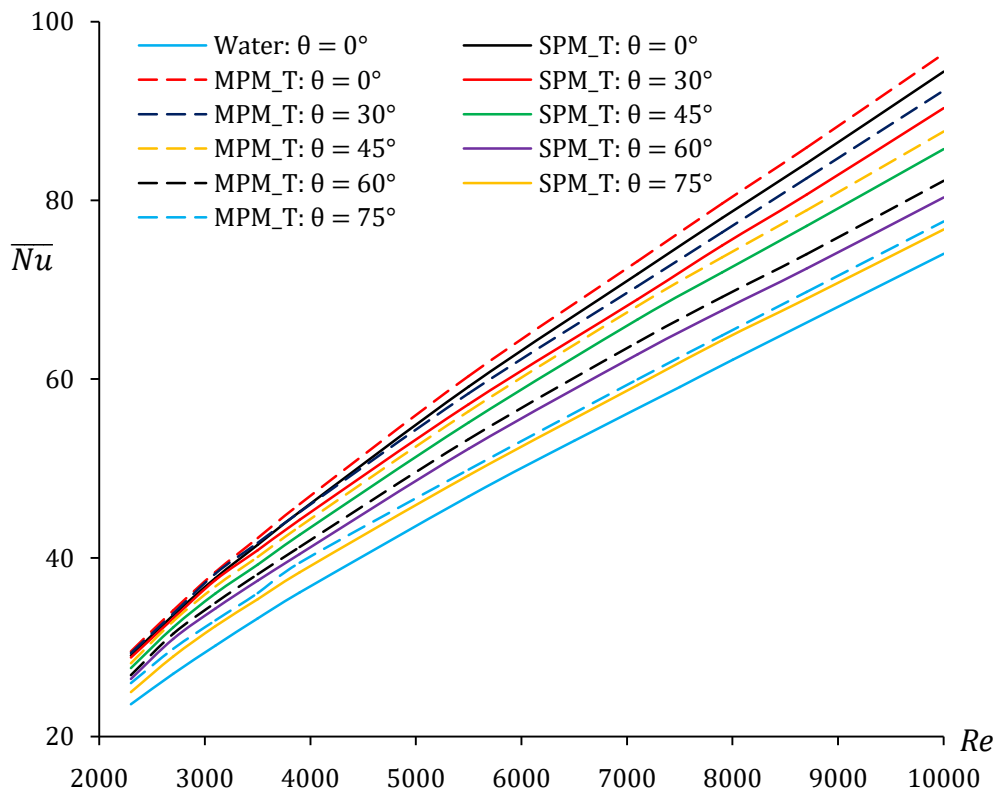
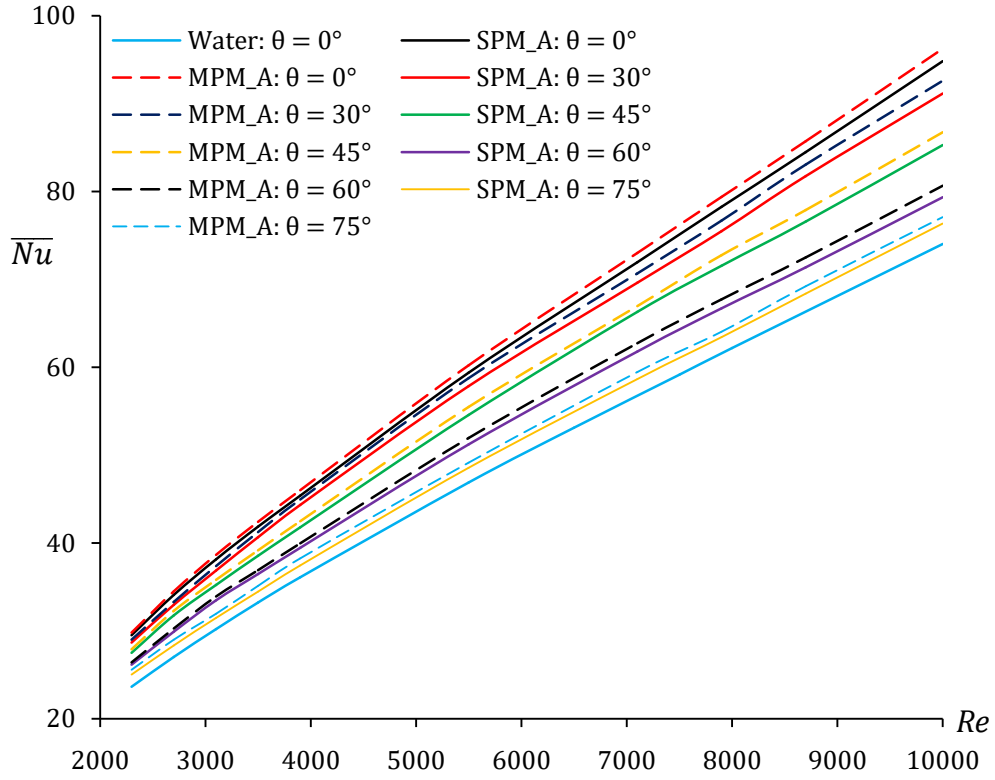


Figure 16: Variations of Average Nusselt number with different Reynolds numbers for different inclination angles,  $\theta = 0^\circ$  to  $75^\circ$

## References

- [1] G. Saha, M.C. Paul, Numerical analysis of heat transfer behaviour of water based  $\text{Al}_2\text{O}_3$  and  $\text{TiO}_2$  nanofluids in a circular pipe under the turbulent flow condition, *International Communications in Heat and Mass Transfer*, 56 (2014) 96-108.
- [2] G. Saha, M.C. Paul, Heat transfer and entropy generation of turbulent forced convection flow of nanofluids in a heated pipe, *International Communications in Heat and Mass Transfer*, 61 (2015) 26-36.
- [3] G. Saha, M.C. Paul, Transition of nanofluids flow in pipe using single phase model, (Submitted), 2017.
- [4] Y. He, Y. Jin, H. Chen, Y. Ding, D. Cang, H. Lu, Heat transfer and flow behaviour of aqueous suspensions of  $\text{TiO}_2$  nanoparticles (nanofluids) flowing upward through a vertical pipe, *International Journal of Heat and Mass Transfer* 50 (2007) 2272–2281.
- [5] M. Akbari, A. Behzadmehr, F. Shahraki, Fully developed mixed convection in horizontal and inclined tubes with uniform heat flux using nanofluid, *International Journal of Heat and Fluid Flow* 29 (2008) 545–556.
- [6] R.B. Mansour, N. Galanis, C.T. Nguyen, Experimental study of mixed convection with water- $\text{Al}_2\text{O}_3$  nanofluid in inclined tube with uniform wall heat flux, *International Journal of Thermal Sciences* 50 (2011) 403-410.
- [7] Fluent 6.3 user guide, Fluent Inc., Lebanon, 2006.
- [8] M. Manninen, V. Taivassalo, S. Kallio, On the mixture model for multiphase flow, *Technical research centre of Finland* 288 (1996) 9-18.
- [9] A. Naumann, L. Schiller, A drag coefficient correlation, *Z. Ver. Deutsch. Ing.*, 77 (1935) 318-320.
- [10] F.R. Menter, Two-equation eddy-viscosity turbulence models for engineering applications, *AIAA Journal* 32 (1994) 1598-1605.